Shack–Hartmann wavefront sensing with elongated sodium laser beacons: centroiding versus matched filtering

Luc Gilles and Brent Ellerbroek

We describe modeling and simulation results for the Thirty Meter Telescope on the degradation of sodium laser guide star Shack–Hartmann wavefront sensor measurement accuracy that will occur due to the spatial structure and temporal variations of the mesospheric sodium layer. By using a contiguous set of lidar measurements of the sodium profile, the performance of a standard centroid and of a more refined noise-optimal matched filter spot position estimation algorithm is analyzed and compared for a nominal mean signal level equal to 1000 photodetected electrons per subaperture per integration time, as a function of subaperture to laser launch telescope distance and CCD pixel readout noise. Both algorithms are compared in terms of their rms spot position estimation error due to noise, their associated wavefront error when implemented on the Thirty Meter Telescope facility adaptive optics system, their linear dynamic range, and their bias when detuned from the current sodium profile.

OCIS codes: 010.1080, 010.7350.

1. Introduction

The mesospheric sodium layer is located at a mean altitude of $h_{Na} = 90$ km and has a mean thickness of $\sigma_{Na} = 10$ km. As a result, a sodium laser guide star (LGS) will have perspective elongation, and a Shack–Hartmann wavefront sensor (SH-WFS) subaperture image of such a laser beacon will be elongated. The degree of elongation, θ_{Na}, increases approximately proportionally to the distance between the subaperture and the laser launch telescope (LLT), the thickness of the layer, and decreases proportionally to the inverse of the square of the profile mean altitude: $\theta_{Na} \approx r_{SA}\sigma_{Na}/h_{Na}^2$. For the Thirty Meter Telescope[1] (TMT), the LLT will be located behind the secondary mirror of the telescope, producing radially elongated LGS subaperture focal-plane spots. h_{Na}, σ_{Na}, and the detailed structure of the sodium profile $P_{Na}(h)$ all evolve significantly on time scales of seconds to minutes. For edge subapertures of the TMT ($r_{SA} = 14.5$ m), the average angular size of the sodium layer along the radial direction, is of the order of $\theta_{Na} \sim 3$ arc sec $\geq 3\,\theta_{seeing}$, which is at least three times larger than the seeing-limited angular size $\theta_{seeing} = \lambda_{WFS}/r_0(\lambda_{WFS})$ of the transverse laser beacon intensity pattern at the laser focus on the sodium layer.

Here we analyze the impact of these radially elongated and temporally varying LGS spots on the measurement accuracy, the associated wavefront error, and the linear dynamic range of the standard centroid algorithm and of a more refined noise-optimal matched filter spot position estimation algorithm for the TMT facility adaptive optics (AO) system. The results presented are based on a contiguous set of 88 lidar sodium profile measurements with temporal and spatial resolutions of 72 s and 24 m, respectively.[2] For square subapertures of size equal to $d_{SA} = 0.5$ m at the primary mirror and integration times of the order of 1 ms, which correspond to the TMT baseline AO system design, a 17 W cw sodium laser is anticipated to provide a mean photon return, yielding of the order of $N = 10^3$ photodetected electrons per sensing subaperture per integration time.[3] This level of signal is assumed throughout the paper and is the requirement currently imposed upon the TMT LGS facility.

It is found that the rms spot position estimation error due to noise is significantly increased at the edge of the TMT aperture due to the impact of LGS elongation, but the effect can be reduced with noise-optimal matched filter processing. This is particularly true when CCD readout noise is nonzero. The

The authors are with the Thirty Meter Telescope Project Office, 1200 East California Boulevard, Mail Code 102-8, Pasadena, California 91125. L. Gilles's e-mail address is lgilles@caltech.edu.

Received 21 November 2005; accepted 10 April 2006; posted 17 April 2006 (Doc. ID 65931).

0003-6935/06/256568-09$15.00/0

wavefront error for the TMT baseline AO system employing 16×4 CCD arrays per subaperture is of the order of 32 nm in the absence of read noise and 45 nm with 5 electrons rms read noise per pixel per read for the matched filter algorithm. The additional root-sum-square (rss) wavefront error for a centroid algorithm is of the order of 14 and 55 nm, respectively.

In terms of linear dynamic range, the centroid algorithm provides 2–3 times more dynamic range than the matched filter, but the effect is expected to be small since (i) the null point for each LGS WFS subaperture may be calibrated to account for noncommon path wavefront aberrations without dynamic range degradation, and (ii) the time-varying residual tip–tilt subaperture wavefront aberrations due to atmospheric turbulence is expected to be smaller than the dynamic ranges in question.

The paper is organized as follows: Section 2 provides an overview of the LGS SH-WFS subaperture spot model. Subsections 2.B and 2.C present the centroid and the matched filter spot position estimation algorithms, respectively. Sample numerical results are presented in Section 3. Finally, Section 4 concludes the study.

2. Laser Guide Star Shack–Hartmann Wavefront Sensor Spot Model and Spot Position Estimation Algorithms

A. Spot Model

The LGS SH-WFS subaperture spot model developed for this study was inspired by a similar model proposed by Ellerbroek.[4,5] The continuous subaperture average spot will be denoted $i(\theta_x, \theta_y)$, where θ_x and θ_y denote the angular position coordinates in the subaperture focal plane along the horizontal and vertical directions. In the angular frequency domain, the subaperture spot spectrum will be denoted $\hat{i}(u_x, u_y)$, where u_x and u_y denote the angular frequency coordinates along the horizontal and vertical directions. Isoplanatic conditions are assumed to approximately hold, so that $i(\theta_x, \theta_y)$ can be modeled as the convolution of the subaperture point-spread function, denoted $\mathrm{PSF}_{\mathrm{SA}}(\theta_x, \theta_y)$, with the beacon object, denoted $i_{\mathrm{beacon}}(\theta_x, \theta_y)$:

$$i(\theta_x,\ \theta_y) = \mathrm{PSF}_{\mathrm{SA}}(\theta_x,\ \theta_y) * i_{\mathrm{beacon}}(\theta_x,\ \theta_y). \tag{1}$$

The subaperture PSF is modeled like a short-exposure Kolmogorov turbulence degraded PSF, and the beacon object as the convolution of the laser beam transverse cross section at the laser focus on the sodium layer with a geometric image of the sodium profile, denoted $i_{\mathrm{Na}}(\theta_x, \theta_y)$, modeling the depth of the sodium layer. Invoking reciprocity, the laser beam transverse cross section at the laser focus on the sodium laser is modeled as the LLT aperture PSF reflected about the origin, denoted $\mathrm{PSF}_{\mathrm{LLT}}(\theta_x, \theta_y)$. As for the sensing subaperture, the LLT PSF is modeled like a short-exposure Kolmogorov turbulence degraded PSF. Thus we have

$$i_{\mathrm{beacon}}(\theta_x,\ \theta_y) = \mathrm{PSF}_{\mathrm{LLT}}(-\theta_x,\ -\theta_y) * i_{\mathrm{Na}}(\theta_x,\ \theta_y). \tag{2}$$

The beacon object is proportional to signal level N, and it is normalized such that the integral of the subaperture spot over an infinite focal plane is equal to N:

$$\int_{-\infty}^{\infty} \mathrm{d}\theta_x \int_{-\infty}^{\infty} \mathrm{d}\theta_y i(\theta_x,\ \theta_y) = N. \tag{3}$$

Invoking the convolution theorem, the angular frequency spectrum of the subaperture spot is expressed as a product of the respective spectra:

$$\hat{i}(u_x,\ u_y) = \mathrm{OTF}_{\mathrm{SA}}(u_x,\ u_y)\hat{i}_{\mathrm{beacon}}(u_x,\ u_y), \tag{4}$$

$$\hat{i}_{\mathrm{beacon}}(u_x,\ u_y) = \mathrm{OTF}^{*}_{\mathrm{LLT}}(u_x,\ u_y)\hat{i}_{\mathrm{Na}}(u_x,\ u_y). \tag{5}$$

The sensing subaperture and LLT aperture PSFs are modeled like the inverse Fourier transform of the respective short-exposure Kolmogorov turbulence degraded OTFs:

$$\mathrm{PSF}_{\mathrm{SA(LLT)}}(\theta_x,\ \theta_y;\ \lambda) = \frac{\mathcal{F}^{-1}\{\mathrm{OTF}_{\mathrm{SA(LLT)}}(u_x,\ u_y;\ \lambda)\}}{\displaystyle\int_{-\infty}^{\infty} \mathrm{d}u_x \int_{-\infty}^{\infty} \mathrm{d}u_y \mathrm{OTF}^{\mathrm{DL}}_{\mathrm{SA(LLT)}}(u_x,\ u_y;\ \lambda)}, \tag{6}$$

$$\mathrm{OTF}_{\mathrm{SA(LLT)}}(u_x,\ u_y;\ \lambda) = \frac{\displaystyle\int_{-\infty}^{\infty} \mathrm{d}x \int_{-\infty}^{\infty} \mathrm{d}y\, f_{\mathrm{SA(LLT)}}}{\displaystyle\int_{-\infty}^{\infty} \mathrm{d}x \int_{-\infty}^{\infty} \mathrm{d}y\, |U_{\mathrm{SA(LLT)}}(x,\ y)|^2}, \tag{7}$$

$$f_{\mathrm{SA(LLT)}} = U_{\mathrm{SA(LLT)}}(x, y; \lambda) U^{*}_{\mathrm{SA(LLT)}}(x + \lambda u_x,\ y + \lambda u_y;\ \lambda) \times \exp\left[-\frac{1}{2}\left(\frac{2\pi}{\lambda}\right)^2 D_{\overline{\mathrm{OPD}}_{\mathrm{SA(LLT)}}}(x,\ y;\ x + \lambda u_x,\ y + \lambda u_y) \right], \tag{8}$$

where $U_{\mathrm{SA(LLT)}}$ denotes the subaperture (LLT aperture) field amplitude, $D_{\overline{\mathrm{OPD}}_{\mathrm{SA(LLT)}}}$ is the piston tip–tilt removed Kolmogorov optical path difference (OPD) structure function, (x, y) is the spatial coordinate of a point in the subaperture (LLT aperture), and $\mathrm{OTF}^{\mathrm{DL}}_{\mathrm{SA(LLT)}}$ denotes the diffraction limited OTFs. $D_{\overline{\mathrm{OPD}}_{\mathrm{SA(LLT)}}}$ is not a shift-invariant function and must be evaluated numerically as described in Appendix A. $U_{\mathrm{SA(LLT)}}$ is expressed as follows:

$$U_{\mathrm{SA(LLT)}}(x,\ y;\ \lambda) = W_{\mathrm{SA(LLT)}}(x,\ y) \times \exp\left[j\,\frac{2\pi}{\lambda}\,\mathrm{OPD}_{\mathrm{SA(LLT)}}(x,\ y) \right], \tag{9}$$

$$W_{\mathrm{SA}}(x,\ y) = \mathrm{rect}\left(\frac{x}{d_{\mathrm{SA}}}\right)\mathrm{rect}\left(\frac{y}{d_{\mathrm{SA}}}\right), \tag{10}$$

$$\mathrm{OPD}_{\mathrm{SA}}(x,\ y) = \theta_x^{\mathrm{ref}} x + \theta_y^{\mathrm{ref}} y + \theta_x^{\mathrm{in}} x + \theta_y^{\mathrm{in}} y, \tag{11}$$

$$W_{\mathrm{LLT}}(x,\ y) = \mathrm{circ}\left(\frac{2\sqrt{x^2+y^2}}{d_{\mathrm{LLT}}}\right) \times \frac{\exp\left[-(x^2+y^2)/(2\sigma_{\mathrm{laser}}^2)\right]}{2\pi\sigma_{\mathrm{laser}}^2}, \tag{12}$$

$$\mathrm{OPD}_{\mathrm{LLT}}(x,\ y) = 0, \tag{13}$$

where $(\theta_x^{\mathrm{ref}}, \theta_y^{\mathrm{ref}})$ denotes the angular coordinates of the subaperture focal plane null point (which will be nonzero to account for WFS noncommon path aberrations), and $(\theta_x^{\mathrm{in}}, \theta_y^{\mathrm{in}})$ denotes the input subaperture Zernike tilt, which is estimated by the centroid and matched filter spot position estimation algorithms detailed in Subsections 2.B and 2.C. The $1/e^2$ laser beam intensity diameter is equal to $2\sqrt{2}\sigma_{\mathrm{laser}}$. The use of short-exposure Kolmogorov turbulence degraded OTFs is based on the assumption that (i) the LGS SH-WFS and laser pointing loop operate in closed loop and are perfectly tip–tilt compensated, and (ii) d_{SA} and d_{LLT} are small so that the Kolmogorov statistics approximately hold.

Finally, expressing the Cartesian coordinates of a given subaperture in terms of its polar coordinates, $x_{\mathrm{SA}} = r_{\mathrm{SA}}\cos(\varphi_{\mathrm{SA}})$, $y_{\mathrm{SA}} = r_{\mathrm{SA}}\sin(\varphi_{\mathrm{SA}})$, it is convenient to introduce locally rotated angular coordinates $(\theta_{\parallel}, \theta_{\perp})$, related to (θ_x, θ_y) by a rotation:

$$\begin{bmatrix}\theta_{\parallel}\\ \theta_{\perp}\end{bmatrix} = \mathrm{Rot}_{\mathrm{SA}}(-\varphi_{\mathrm{SA}})\begin{bmatrix}\theta_x\\ \theta_y\end{bmatrix}, \tag{14}$$

$$\mathrm{Rot}_{\mathrm{SA}}(\varphi_{\mathrm{SA}}) = \begin{bmatrix}\cos(\varphi_{\mathrm{SA}}) & \sin(\varphi_{\mathrm{SA}})\\ -\sin(\varphi_{\mathrm{SA}}) & \cos(\varphi_{\mathrm{SA}})\end{bmatrix}. \tag{15}$$

Note that the $\parallel$ axis points thus from the LLT to the subaperture of interest, and the $\perp$ axis is orthogonal to that direction (see Fig. 1). These two directions will be referred to hereafter as radial and azimuthal. The geometrical image of the sodium profile $P_{\mathrm{Na}}(h)$ at a distance r_{SA} from the LLT is then modeled as follows:

$$i_{\mathrm{Na}}(\theta_x,\ \theta_y) = \frac{1}{r_{\mathrm{SA}}}\,\delta(\theta_{\perp})P_{\mathrm{Na}}(h(\theta_{\parallel}) + h_{\mathrm{Na}}), \tag{16}$$

$$h(\theta_{\parallel}) \approx \delta h + \frac{h_{\mathrm{LGS}}^2\theta_{\parallel}}{r_{\mathrm{SA}}}, \tag{17}$$

$$\delta h = h_{\mathrm{LGS}} - h_{\mathrm{Na}}, \tag{18}$$

where $\theta_{\parallel}$ and $\theta_{\perp}$ are given by Eq. (14), h_{Na} is the centroid of the sodium profile, and h_{LGS} denotes the LGS SH-WFS focus altitude.

This study addresses the impacts of the sodium layer structure and structural variability but does not address the impacts of a temporal lag on refocusing the laser to the correct mean sodium layer altitude, hence we assume hereafter that $\delta h = h_{\mathrm{LGS}} - h_{\mathrm{Na}} = 0$. In the angular frequency domain, the sodium profile image spectrum is given by the following expression:

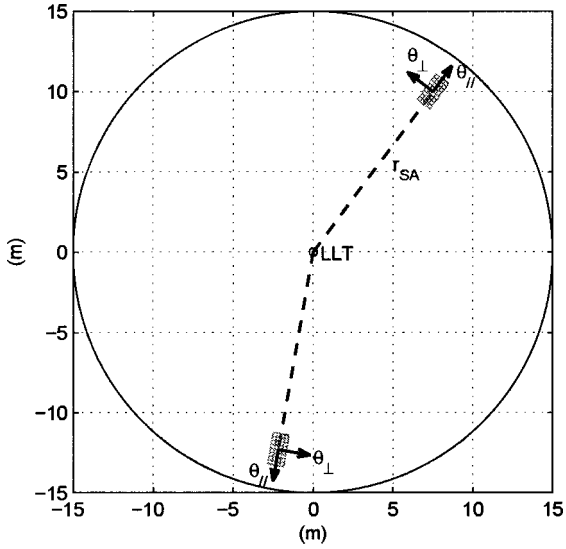

Fig. 1. Illustration of subaperture focal-plane radial geometry CCD arrays.

$$\hat{i}_{\mathrm{Na}}(u_x,\ u_y) = \frac{1}{h_{\mathrm{LGS}}^2}\,\hat{P}_{\mathrm{Na}}\left(f = \frac{x_{\mathrm{SA}}u_x + y_{\mathrm{SA}}u_y}{h_{\mathrm{LGS}}^2}\right) \times \exp(j2\pi f h_{\mathrm{LGS}}). \tag{19}$$

Higher-order effects generated by the 3D LGS that are not included in the model are speckle noise and depth of focus.

Pixel intensities averaged over the Poisson photon arrival statistics and over the normally distributed readout noise are obtained by integrating the continuous LGS SH-WFS subaperture spot $i(\theta_x, \theta_y)$ over each CCD pixel bin $B^{(k)}(\theta_x, \theta_y)$. In vector notation, we have

$$\vec{I}^{\mathrm{avg}} = \int_{-\infty}^{\infty} \mathrm{d}\theta_x \int_{-\infty}^{\infty} \mathrm{d}\theta_y i(\theta_x,\ \theta_y)\vec{B}(\theta_x,\ \theta_y) \tag{20}$$

$$= \int_{-\infty}^{\infty} \mathrm{d}u_x \int_{-\infty}^{\infty} \mathrm{d}u_y \hat{i}(u_x,\ u_y)\hat{\vec{B}}^*(u_x,\ u_y), \tag{21}$$

where the last equality follows from the fact that the Fourier transform is a unitary transformation. Pixel bins are modeled as square boxes of angular subtense θ_{pix}, with radial and azimuthal coordinate vectors $\vec{\theta}_{\parallel}$ and $\vec{\theta}_{\perp}$ in the locally rotated frame, blurred by a Gaussian response function modeling charge diffusion:

$$\vec{B}(\theta_x,\ \theta_y) = \mathrm{rect}\left(\frac{\theta_\parallel - \vec{\theta}_\parallel}{\theta_{\mathrm{pix}}}\right)\mathrm{rect}\left(\frac{\theta_\perp - \vec{\theta}_\perp}{\theta_{\mathrm{pix}}}\right) * \frac{\exp\left[-\left(\theta_\parallel^2 + \theta_\perp^2\right)/\left(2\theta_{\mathrm{blur}}^2\right)\right]}{2\pi\theta_{\mathrm{blur}}^2}, \tag{22}$$

where $\theta_\parallel$ and $\theta_\perp$ are again given by Eq. (14).

Noisy pixel intensities are obtained by adding a noise term to the above average pixel intensities as follows:

$$\vec{I} = \vec{I}^{\mathrm{avg}} + \vec{\eta}, \tag{23}$$

$$\vec{\eta} = \mathrm{Poisson}\left(\vec{I}^{\mathrm{avg}}\right) - \vec{I}^{\mathrm{avg}} + \sigma_e\,\mathrm{Normal}\left(\vec{0},\ \mathcal{I}\right), \tag{24}$$

where $\mathcal{I}$ is the identity matrix. Note that $\vec{\eta}$ has a zero ensemble mean, and a diagonal covariance matrix equal to

$$C_\eta = \langle\vec{\eta}\vec{\eta}^T\rangle - \langle\vec{\eta}\rangle\langle\vec{\eta}\rangle^T = \mathrm{diag}\left(\vec{I}^{\mathrm{avg}} + \sigma_e^2\right). \tag{25}$$

A subaperture focal-plane CCD array with $N_{\mathrm{pix}}^{\parallel} \times N_{\mathrm{pix}}^{\perp}$ pixels is expressed as the sum of the individual pixel bins $B^{(k)}(\theta_x, \theta_y)$. Integrating the subaperture spot over the total field of view (FOV) of the detector array yields the average signal level multiplied by a leakage factor:

$$\vec{1}^T\vec{I}^{\mathrm{avg}} = \int_{-\infty}^{\infty} \mathrm{d}\theta_x \int_{-\infty}^{\infty} \mathrm{d}\theta_y i(\theta_x,\ \theta_y)\vec{1}^T\vec{B}(\theta_x,\ \theta_y) = \gamma N, \tag{26}$$

where $\gamma \le 1$ is the leakage factor, i.e., the energy loss factor due to photons falling outside the CCD array. The subaperture signal-to-noise ratio (SNR) is then equal to

$$\mathrm{SNR} = \frac{\vec{1}^T\vec{I}^{\mathrm{avg}}}{\sqrt{\mathrm{Tr}(C_\eta)}} = \frac{\gamma N}{\sqrt{\gamma N + N_{\mathrm{pix}}^{\parallel} N_{\mathrm{pix}}^{\perp}\,\sigma_e^2}}. \tag{27}$$

B. Centroid Algorithm

The centroid algorithm has been extensively used in combination with 2×2 pixel arrays known as quadrant detectors or quad cells. A detailed analysis of the algorithm's noise properties was presented in this context by Tyler and Fried[6] in their seminal 1982 paper. This material is briefly reviewed below within the framework of an arbitrary CCD array geometry with $N_{\mathrm{pix}}^{\parallel} \times N_{\mathrm{pix}}^{\perp}$ pixels and an arbitrary subaperture focal plane null point.

The centroid spot position estimate is given by the following expressions:

$$\hat{\theta}_{\parallel(\perp)}^{\mathrm{in}} = \vec{\omega}_{\parallel(\perp)}^T(\alpha\vec{I} - \vec{I}_0^{\,\mathrm{avg}}), \tag{28}$$

$$\vec{I}_0^{\,\mathrm{avg}} = \vec{I}^{\mathrm{avg}}\left(\vec{\theta}^{\mathrm{in}} = \vec{0}\right), \tag{29}$$

$$\vec{\omega}_{\parallel(\perp)} = \frac{\theta_{\parallel(\perp)}^B}{\vec{1}^T\vec{I}_0^{\,\mathrm{avg}}}\,\vec{\theta}_{\parallel(\perp)}, \tag{30}$$

$$\alpha = \frac{\vec{1}^T\vec{I}_0^{\,\mathrm{avg}}}{\vec{1}^T\vec{I}}, \tag{31}$$

$$\frac{\theta_{\parallel(\perp)}^B}{\vec{1}^T\vec{I}_0^{\,\mathrm{avg}}} = \left[\left.\frac{\mathrm{d}\vec{\theta}_{\parallel(\perp)}^T\left(\alpha^{\mathrm{avg}}\vec{I}^{\mathrm{avg}} - \vec{I}_0^{\,\mathrm{avg}}\right)}{\mathrm{d}\theta_{\parallel(\perp)}^{\mathrm{in}}}\right|_{\theta_{\parallel(\perp)}^{\mathrm{in}}=0}\right]^{-1} \approx \frac{1}{\vec{g}_{\parallel(\perp)}^T\vec{\theta}_{\parallel(\perp)}}, \tag{32}$$

$$\vec{g}_{\parallel(\perp)} = \left.\frac{\partial\vec{I}^{\mathrm{avg}}}{\partial\theta_{\parallel(\perp)}^{\mathrm{in}}}\right|_{\theta_{\parallel(\perp)}^{\mathrm{in}}=0}. \tag{33}$$

$\theta_{\parallel(\perp)}^B$ in Eq. (30) and $\vec{g}_{\parallel(\perp)}$ in Eq. (33) denote, respectively, the centroid gain and the radial and azimuthal slopes of the average pixel intensity transfer curves at null. The latter can be estimated in practice by continually dithering the laser beacon on the sky and can be updated on slow time scales of a few seconds.

It should be pointed out that a spot position estimation bias occurs in the radial direction if the centroid algorithm is not updated rapidly enough to track the variations in the shape of the sodium profile. Mathematically, this bias is expressed as follows:

$$\hat{\theta}_{\mathrm{bias}}(t;\ t+\delta) = \vec{\omega}_{\parallel(\perp)}^T(t)\left[\alpha(t;\ t+\delta)\vec{I}_0^{\,\mathrm{avg}}(t+\delta) - \vec{I}_0^{\,\mathrm{avg}}(t)\right], \tag{34}$$

$$\alpha(t;\ t+\delta) = \frac{\vec{1}^T\vec{I}_0^{\,\mathrm{avg}}(t)}{\vec{1}^T\vec{I}_0^{\,\mathrm{avg}}(t+\delta)}. \tag{35}$$

Note that if $\vec{I}_0^{\,\mathrm{avg}}(t+\delta)$ is simply proportional to $\vec{I}_0^{\,\mathrm{avg}}(t)$, the spot position estimation bias is equal to zero. A rough estimate of the telescope full-aperture wavefront error due to a nonzero bias can be obtained by reconstructing the wavefront at the subaperture resolution and summing up radially the biases for each subaperture from the LLT to the edge of the aperture. In integral notation, this is expressed as follows:

$$\hat{\phi}_{\mathrm{bias}}(r) = \int_0^r \mathrm{d}r'\hat{\theta}_{\mathrm{bias}}(r'). \tag{36}$$

The piston removed and piston-focus removed wavefronts can then be computed by using the usual formulas:

$$\hat{\phi}^{(1)}_{\text{bias}}(r) = \hat{\phi}_{\text{bias}}(r) - c_1 Z_1\left(\frac{2r}{D}\right), \tag{37}$$

$$\hat{\phi}^{(4)}_{\text{bias}}(r) = \hat{\phi}_{\text{bias}}{}^{(1)}(r) - c_4 Z_4\left(\frac{2r}{D}\right), \tag{38}$$

$$c_{1(4)} = \frac{\int_0^{2\pi} \mathrm{d}\varphi \int_0^{D/2} r\mathrm{d}r \hat{\phi}_{\text{bias}}(r) Z_{1(4)}(2r/D)}{\pi D^2/4}, \tag{39}$$

where $Z_{1(4)}$ denote the Zernike piston and focus modes. The rms error due to the biases is finally expressed as

$$\sigma^2_{1(4)} = \frac{\int_0^{2\pi} \mathrm{d}\varphi \int_0^{D/2} r\mathrm{d}r \left\{\hat{\phi}^{(4)}_{\text{bias}}(r)\right\}^2}{\pi D^2/4}. \tag{40}$$

Due to photon and readout noise, the centroid estimate in Eq. (28) is a random variable, whose variance at the null point, known as the centroid noise propagation, is equal to the following expression:

$$\sigma^2_{\theta_{\|(\perp)}} = \left(\frac{\theta^B_{\|(\perp)}}{\vec{1}^T \vec{I}_0{}^{\text{avg}}}\right)^2 \text{var}\left[\vec{\theta}^T_{\|(\perp)}\left(\alpha \vec{I}_0{}^{\text{avg}} + \alpha\vec{\eta} - \vec{I}_0{}^{\text{avg}}\right)\right], \tag{41}$$

$$\alpha = \frac{1}{1+\epsilon} \approx 1 - \epsilon, \tag{42}$$

$$\epsilon = \frac{\vec{1}^T \eta}{\vec{1}^T \vec{I}_0{}^{\text{avg}}}. \tag{43}$$

After a little algebra, the following expressions are obtained:

$$\sigma^2_{\theta_{\|(\perp)}} = \left(\theta^B_{\|(\perp)}\right)^2 \left[\frac{\xi_{\|(\perp)}}{\text{SNR}^2\left(\vec{\theta}^{\text{in}} = \vec{0}\right)} + \frac{q^2_{\|(\perp)}}{\text{SNR}^2\left(\vec{\theta}^{\text{in}} = \vec{0}\right)} - 2\,\frac{q^2_{\|(\perp)}}{\vec{1}^T \vec{I}_0{}^{\text{avg}}}\right], \tag{44}$$

$$q_{\|(\perp)} = \vec{\theta}^T_{\|(\perp)} \frac{\vec{I}_0{}^{\text{avg}}}{\vec{1}^T \vec{I}_0{}^{\text{avg}}}, \tag{45}$$

$$\xi_{\|(\perp)} = \frac{\text{Tr}\left[\vec{\theta}_{\|(\perp)} \vec{\theta}^T_{\|(\perp)} C_{\text{mod}}\right]}{\text{Tr}(C_{\text{mod}})} = \frac{\sum_k \left[\theta^{(k)}_{\|(\perp)}\right]^2 \left[I_0{}^{\text{avg}(k)} + \sigma_e{}^2\right]}{\sum_k \left[\vec{I}_0{}^{\text{avg}(k)} + \sigma_e{}^2\right]}, \tag{46}$$

$$C_{\text{mod}} = C_\eta\left(\vec{\theta}^{\text{in}} = \vec{0}\right). \tag{47}$$

Note that for a quadrant detector, $\xi_{\|(\perp)}$ is simply equal to a quarter of the pixel area subtense.

C. Matched Filter Algorithm

We define a matched filter algorithm by the following noise-weighted least-squares optimization problem:

$$\left(\widehat{\theta^{\text{in}}_{\|}},\ \widehat{\theta^{\text{in}}_{\perp}},\ \widehat{\delta N}\right) = \arg \min_{(\theta^{\text{in}}_{\|},\ \theta^{\text{in}}_{\perp},\delta N)} J\left(\theta^{\text{in}}_{\perp}, \theta^{\text{in}}_{\perp}, \delta N\right), \tag{48}$$

$$J\left(\theta^{\text{in}}_{\|},\ \theta^{\text{in}}_{\perp},\ \delta N\right) = \vec{y}^T C^{-1}_{\text{mod}} \vec{y}, \tag{49}$$

$$\vec{y} = \vec{I} - \left(\vec{I}_0{}^{\text{avg}} + \vec{g}_{\|}\theta^{\text{in}}_{\|} + \vec{g}_{\perp}\theta^{\text{in}}_{\perp} + \frac{\vec{I}_0{}^{\text{avg}}}{N}\,\delta N\right), \tag{50}$$

$$C_{\text{mod}} = C_\eta\left(\theta^{\text{in}}_{\|} = 0,\ \theta^{\text{in}}_{\perp} = 0,\ \delta N = 0\right), \tag{51}$$

where $\vec{g}_{\|(\perp)}$ are given by Eq. (33).

The solution for $\widehat{\theta^{\text{in}}_{\|}}$ and $\widehat{\theta^{\text{in}}_{\perp}}$ is given by the following expressions:

$$\bar{\theta}^{\text{in}}_{\|(\perp)} = \vec{\omega}^T_{\|(\perp)}\left(\vec{I} - \vec{I}_0{}^{\text{avg}}\right), \tag{52}$$

$$\vec{\omega}_{\|} = \sigma^2_{\theta_{\|}} C^{-1}_{\text{mod}}\left(\vec{g}_{\|} - \mu \vec{I}_0{}^{\text{avg}}\right), \tag{53}$$

$$\mu = \frac{\vec{g}_{\|}{}^T C^{-1}_{\text{mod}} \vec{I}_0{}^{\text{avg}}}{\vec{I}_0{}^{\text{avg}T} C^{-1}_{\text{mod}} \vec{I}_0{}^{\text{avg}}}, \tag{54}$$

$$\vec{\omega}_{\perp} = \sigma^2_{\theta_{\perp}} C^{-1}_{\text{mod}} \vec{g}_{\perp}. \tag{55}$$

The matched filter noise propagation coefficients are expressed as follows:

$$\sigma^2_{\theta_{\|}} = \frac{1}{\vec{g}_{\|}{}^T C^{-1}_{\text{mod}}\left(\vec{g}_{\|} - \mu \vec{I}_0{}^{\text{avg}}\right)}, \tag{56}$$

$$\sigma^2_{\theta_{\perp}} = \frac{1}{\vec{g}^T_{\perp} C^{-1}_{\text{mod}} \vec{g}_{\perp}}. \tag{57}$$

Equations (52)–(57) follow from the following symmetries of vectors $\vec{g}_{\|}$, $\vec{g}_{\perp}$, and $\vec{I}_0{}^{\text{avg}}$ when displayed as $N^{\|}_{\text{pix}} \times N^{\perp}_{\text{pix}}$ arrays:

(i) Array $(\vec{g}_{\|})$ is symmetric along the $\perp$ direction, i.e., its rows are identical.

(ii) Array $(\vec{g}_{\perp})$ is antisymmetric along the $\perp$ direction, i.e., $\vec{g}^T_{\perp}\vec{1} = 0$. In particular, $\vec{g}^T_{\perp}\vec{g}_{\|} = 0$.

(iii) Array $(\vec{I}_0{}^{\text{avg}})$ is symmetric along the $\perp$ direction, i.e., its rows are identical. In particular, $\vec{g}^T_{\perp} C^{-1}_{\text{mod}} \vec{I}_0{}^{\text{avg}} = \vec{g}^T_{\perp} C^{-1}_{\text{mod}} \vec{g}_{\|} = 0$.

Finally, as for the centroid algorithm, a spot position estimation bias occurs in the radial direction if the matched filter algorithm is not updated rapidly

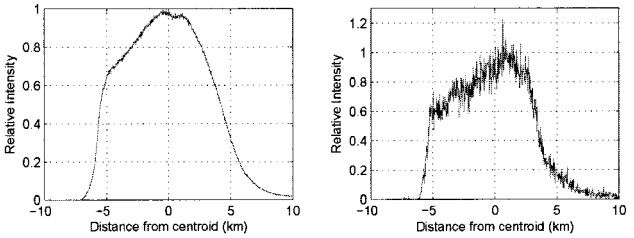

Fig. 2. Left panel, mean sodium profile obtained by averaging and centering 88 contiguous frames of lidar measurements of the sodium layer with spatial resolution equal to 24 m (Ref. 2). Right panel, sample sodium profile frame.

enough to track the variations in the shape of the sodium profile. Note that the parameter μ in Eq. (53) ensures that $\hat{\theta}_{\text{bias}} = 0$ and $\widehat{\delta N} = \delta N$ if $\vec{I} = (N + \delta N)/N\vec{I}_0^{\text{avg}}$.

3. Simulation Results

Figure 2 displays the mean sodium profile obtained by averaging and centering 88 contiguous frames of lidar measurements with a spatial resolution equal to 24 m (Ref. 2) as well as a sample sodium profile frame.

Figure 3 displays the Nyquist sampled short-exposure subaperture and LLT aperture PSFs. The subaperture size was taken equal to $d_{\text{SA}} = 0.5$ m (order 60×60 wavefront sensor), the LLT diameter equal to $d_{\text{LLT}} = d_{\text{SA}} = 0.5$ m, and the $1/e^2$ Gaussian laser beam intensity diameter equal to $0.6d_{\text{LLT}} = 0.3$ m. The Fried parameter was chosen equal to $r_0(\lambda_0 = 500\,\text{nm}) = 0.15$ m. Note that the LLT Strehl ratio (SR) is in excellent agreement with Maréchal's approximation, $\text{SR}(\lambda_{\text{WFS}}) \approx \exp(-\sigma^2)$, where $\sigma^2 = 0.134[d_{\text{LLT}}/r_0(\lambda_{\text{WFS}})]^{5/3}$ is the piston tip–tilt removed Kolmogorov phase variance in radians squared. PSFs were computed in the Fourier domain by using 64×64 FFT grids.

Figure 4 displays the Nyquist sampled normalized average beacon radial and the azimuthal cross sections as seen from a subaperture 1 and 14.5 m away from the LLT, together with the total subaperture spot obtained by convolving the beacon with the short-exposure subaperture PSF. The FWHM of the radial and azimuthal cross sections of the edge sub-

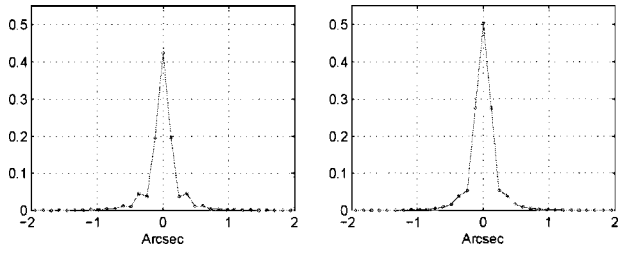

Fig. 3. Left panel, Nyquist sampled subaperture short-exposure PSF. Right panel, Nyquist sampled LLT aperture short-exposure PSF. The subaperture size was taken equal to $d_{\text{SA}} = 0.5$ m (order 60×60 wavefront sensor), the LLT diameter equal to $d_{\text{LLT}} = d_{\text{SA}} = 0.5$ m, and the $1/e^2$ Gaussian laser beam diameter equal to $0.6\,d_{\text{LLT}} = 0.3$ m. These quantities were computed in the Fourier domain by using a 32×32 subaperture grid embedded into a 64×64 FFT grid. The Fried parameter is $r_0(\lambda_0 = 500\,\text{nm}) = 0.15$ m and the turbulence outer scale is infinite.

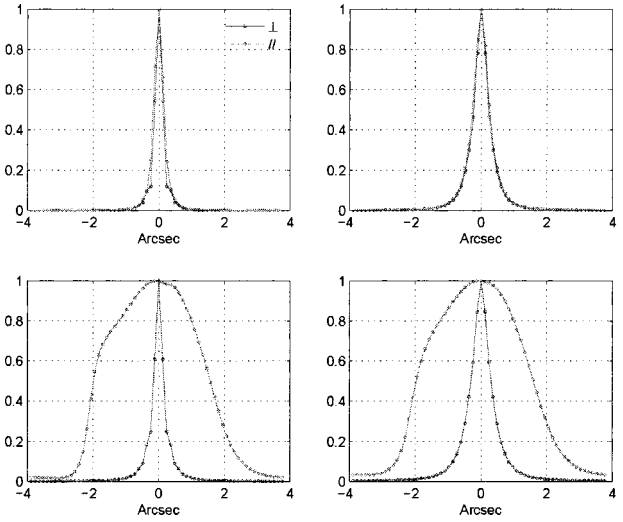

Fig. 4. Left panels, Nyquist sampled normalized average beacon radial and azimuthal cross sections as seen from a subaperture 1 and 14.5 m away from the LLT. Right panels, total subaperture spot obtained by convolving the beacon with the short-exposure subaperture PSF at a distance of 1 and 14.5 m.

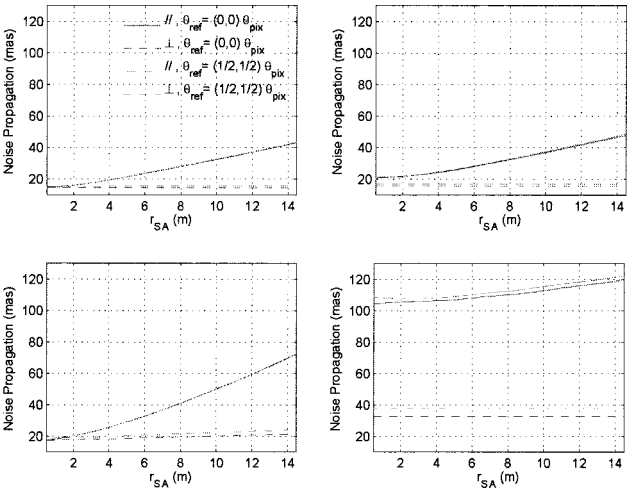

Fig. 5. Radial and azimuthal photon and readout noise propagation levels associated with the matched filter (left panels) and centroid spot (right panels) position estimators, as a function of the subaperture-to-LLT separation. These curves are for the median sodium profile displayed in Fig. 2. The beacon brightness has been scaled to provide a mean signal level equal to $N = 10^3$ photodetected electrons per subaperture per integration time, and the cases of $\sigma_e = 0$ (top) and $\sigma_e = 5$ (bottom) electrons rms readout noise are compared for a 16×4 subaperture focal-plane CCD pixel array with $\theta_{\text{pix}} = 0.5$ arc sec pixel subtense and $\theta_{\text{blur}} = \theta_{\text{pix}}/4$ pixel blurring due to charge diffusion. The corresponding SNRs are of the order of 31 and 19, respectively. Blue and red curves refer to the null point set, respectively, at the origin (center) of the subaperture focal plane and at a null position shifted by half a pixel in both the radial and azimuthal directions (as might be the case with sample noncommon path wavefront errors). Such a null point offset has no impact on the noise properties of the algorithms.

Table 1. Radial, Azimuthal, and rss Photon and Readout Noise Propagation Levels[a]

Spot Position Estimation Algorithm	Read Noise per Pixel per Read (electrons)	Measurement Noise (mas) Central Subaperture			Measurement Noise (mas) Edge Subaperture		
		Radial	Azimuthal	rss	Radial	Azimuthal	rss
Centroid	0	21	16	26	48	16	50
	5	104	33	109	119	33	124
Matched Filter	0	15	15	21	43	15	46
	5	18	18	25	72	22	76

[a]The levels are read at $r_{SA} = 0.5$ m and $r_{SA} = 14.5$ m for the centroid and matched filter spot position estimators operating on the same CCD array and mean signal level as in Fig. 5.

aperture spot is of the order of 3.5 and 0.8 arc sec, respectively.

Figure 5 shows the radial and azimuthal rms noise propagation levels for the matched filter and centroid spot position estimators, as a function of subaperture-to-LLT separation. These curves are for the median sodium profile displayed in Fig. 2. The beacon brightness has been scaled to provide a mean signal level of $N = 10^3$ photodetected electrons per subaperture per integration time, which is the requirement currently imposed upon the TMT LGS facility, and the cases of $\sigma_e = 0$ and $\sigma_e = 5$ electrons rms readout noise are compared for a 16×4 subaperture focal-plane CCD pixel array with $\theta_{pix} = 0.5$ arc sec pixel subtense and $\theta_{blur} = \theta_{pix}/4$ pixel blurring modeling charge diffusion. The corresponding SNRs are of the order of 31 and 19, respectively. It is seen that the spot position estimation error due to noise is significantly increased at the edge of the TMT aperture due to the impact of LGS elongation, but the effect can be reduced through the use of the noise-optimal matched filter. This is particularly true when the detector readout noise is nonzero. It is also seen that shifting the null point from the origin (center) of the subaperture focal plane to half a pixel in both the radial and the azimuthal directions (as might be the case with sample noncommon path wavefront errors) only marginally degrades the noise properties of the algorithms. These results are summarized for a central and an edge subaperture in Table 1. The wavefront error due to the noise has been computed for the TMT facility AO system and is displayed in Table 2. The system consists of 5 LGSs in a 35 arc sec radius and 1 LGS on axis, order 60×60 sensing and correction (0.5 m subapertures and 0.5 m actuator pitch), 16×4 CCD arrays per subaperture, 1 tip–tilt focus natural guide star WFS on axis, and two deformable mirrors conjugate to ground and 12 km, respectively. Wavefront control is done by using a double-pole integrator with a gain of 0.5 operating in pseudo-open loop.[7] The error budget has been computed by subtracting in quadrature noise-free from noisy closed-loop Monte Carlo simulation results by using the same mean sodium profile as in Fig. 5. Noise-free simulations were run with a minimum variance wavefront reconstructor incorporating 15 mas subaperture regularization noise. The wavefront error is of the order of 32 nm in the absence of read noise and 45 nm with 5 electrons rms read noise per pixel per read for the matched filter

Table 2. Wavefront Error for the TMT Facility AO System[a]

Spot Position Estimation Algorithm	Read Noise per Pixel per Read (electrons)	Wavefront Error (nm) due to LGS WFS Noise	
		On Axis	10 arc sec FOV Average
Centroid	0	35	32
	5	71	67
Matched Filter	0	32	30
	5	45	42

[a]The error is due to LGS WFS noise for the same signal level, subaperture, CCD geometry, and mean sodium profile as in Fig. 5. The error budget was obtained by subtracting in quadrature noise-free from noisy closed-loop Monte Carlo simulation results. Noise-free simulations were run with a minimum variance wavefront reconstructor incorporating 15 mas subaperture regularization noise.

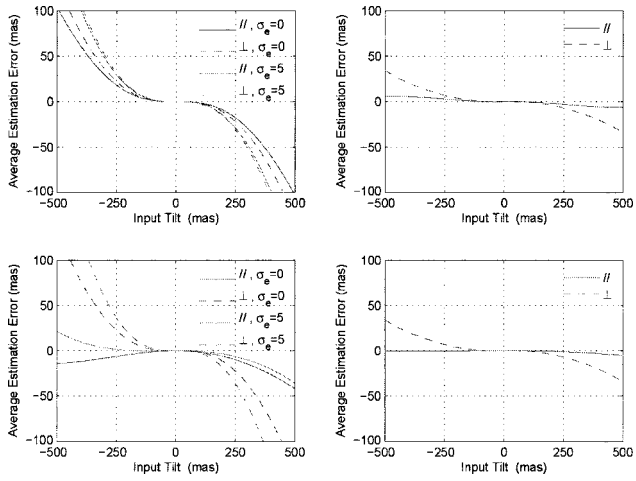

Fig. 6. Average spot position estimation error curves, $\hat{\theta}_{\|(\perp)} - \theta^{in}_{\|(\perp)}$, for a central and an edge subaperture as a function of input tilt level when the null point of the subaperture focal plane is at the origin. The curves for the matched filter algorithm (left panels) are for a mean signal level of 1000 photodetected electrons per subaperture (0.5 and 14.5 m, top and bottom, respectively, for left and right panels) and per integration time and a read noise of either 0 or 5 e rms. For the centroid algorithm (right panels), the curves are independent of signal and read noise levels since the algorithm does not incorporate statistical prior information.

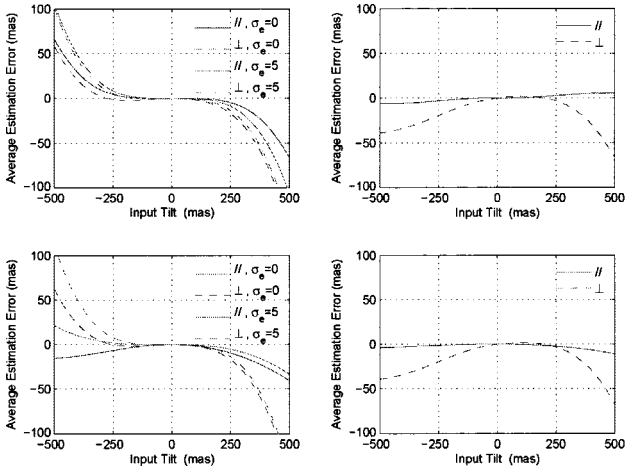

Fig. 7. Same as Fig. 6 but when the null point of the subaperture focal plane is at half a pixel in both radial and azimuthal directions.

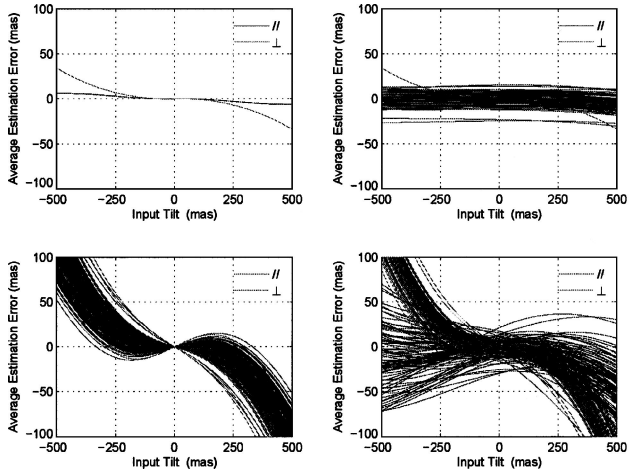

Fig. 8. Average spot position estimation error curves, $\hat{\theta}_{\|(\perp)} - \theta^{\text{in}}_{\|(\perp)}$, for a central and an edge subaperture (0.5 and 14.5 m, left and right panels, respectively, for 1-frame latency) for the centroid (top panels) and matched filter (bottom) algorithms as a function of input tilt level when the null point of the subaperture focal plane is at the origin and the algorithms have 72 s (i.e., 1 frame) update latency. Different curves correspond to the 87 different pairs of contiguous sodium profile frames. Azimuthal curves are identical for all pairs of profiles for the centroid algorithm as a consequence of the symmetry properties of the algorithm.

algorithm. The additional rss wavefront error for a centroid algorithm is of the order of 14 and 55 nm, respectively.

Figures 6 and 7 display the average spot position estimation error, $\hat{\theta}_{\|(\perp)} - \theta^{\text{in}}_{\|(\perp)}$, for a central and an edge subaperture as a function of input subaperture tilt level when the null point is set, respectively, at the origin of the subaperture focal plane and at half a pixel in both the radial and the azimuthal directions. The curves for the matched filter algorithm are for a mean signal level of 1000 photodetected electrons per subaperture and per integration time and a read noise of either 0 or 5 electrons rms. For the centroid algorithm, the curves are independent of signal and read noise levels since the algorithm does not incorporate statistical prior information. The linear dynamic range of the matched filter algorithm is approximately from -100 to $+100$ mas, i.e., approximately from $-\sigma_\alpha/2$ to $+\sigma_\alpha/2$, where σ_α denotes the rms angle of arrival fluctuations over a subaperture of size d_{SA}, i.e., $\sigma_\alpha = \text{PV}_{\text{OPD}}/d_{\text{SA}}$ with $\text{PV}_{\text{OPD}} = \lambda/(2\pi)4\langle a_2^2\rangle^{1/2}$ and $\langle a_2^2\rangle = 0.448(d_{\text{SA}}/r_0)^{5/3}$. Note that these are open-loop results for a single LGS WFS subaperture. The resulting wavefront error for a closed-loop AO system is expected to be small and will be evaluated by using a full wave optics Monte Carlo simulation. The centroid algorithm provides 2–3 times more dynamic range, but the effect is expected to be small. Indeed, shifting the null point to half a pixel in both the radial and the azimuthal directions has no impact on these average spot position estimation error curves. The null point for each LGS WFS subaperture may thus be calibrated to account for noncommon path wavefront aberrations without dynamic range degradation. Moreover, the time-varying residual subaperture wavefront tip–tilt aberrations due to atmospheric turbulence will be smaller than the dynamic ranges quoted above.

Finally, Fig. 8 illustrates sample average spot position estimation error curves for the centroid and matched filter algorithms with 72 s (i.e., 1 frame) update latency. The azimuthal curves are identical for all pairs of profiles for the centroid algorithm as a consequence of the symmetry properties of the algorithm. The rms bias is of the order of 10 mas at $r_{\text{SA}} = 14.5$ m for both algorithms. The full-aperture wavefront error corresponding to this rms bias as given by Eq. (40) is approximately equal to 92 nm. Most of this wavefront error is a focus error. Indeed, the focus removed wavefront error is approximately equal to 12 nm only. Here again, a full wave optics Monte Carlo simulation is required to quantify more precisely the associated wavefront error, and this will be the subject of a future publication.

4. Conclusion

Sodium LGS SH-WFS spot elongation is a significant challenge for future extremely large telescopes such as the TMT. The LGS angular spot size along the elongation direction at the edge of the TMT exceeds three times the angular size of the seeing-limited transverse laser beacon intensity at the laser focus on the sodium layer. Possible approaches to defeat this effect include (i) radial-format CCDs[8] combined with a noise-optimal spot position estimation algorithm[4,5] and (ii) dynamic refocusing. We discussed the first approach. By using a contiguous set of lidar measurements of the sodium profile, the performance of a standard centroid and a more refined noise-optimal matched filter spot position estimation algorithm were analyzed and compared for a nominal mean signal level equal to 1000 photodetected electrons per subaperture per integration time, as a function of subaperture to laser launch telescope sep-

aration distance and CCD pixel readout noise. Both algorithms were compared in terms of their average spot position estimation error due to noise, their wavefront error budget for the TMT facility adaptive optics system, their linear dynamic range, and their bias when detuned from the current sodium profile.

Appendix A

Denoting the subaperture (LLT aperture) piston tip–tilt modal matrix as $M_{\mathrm{SA(LLT)}}$, the projector onto the orthogonal complement to its range space is given by the following expressions:

$$P_{\mathrm{SA(LLT)}} = I - M_{\mathrm{SA(LLT)}} M^{\dagger}_{\mathrm{SA(LLT)}}, \tag{A1}$$

$$M^{\dagger}_{\mathrm{SA(LLT)}} = \left(M^{\mathrm{T}}_{\mathrm{SA(LLT)}} U_{\mathrm{SA(LLT)}} M_{\mathrm{SA(LLT)}}\right)^{-1} \times M^{\mathrm{T}}_{\mathrm{SA(LLT)}} U_{\mathrm{SA(LLT)}}. \tag{A2}$$

Piston tip–tilt removed subaperture (LLT aperture) OPDs are then given by

$$\overrightarrow{\overline{\mathrm{OPD}}}_{\mathrm{SA(LLT)}} = P_{\mathrm{SA(LLT)}} \overrightarrow{\mathrm{OPD}}_{\mathrm{SA(LLT)}}. \tag{A3}$$

The discrete structure function associated with these OPDs is given by the following expression:

$$\left[D_{\overline{\mathrm{OPD}}_{\mathrm{SA(LLT)}}}\right]_{kl} = \left\langle \left[\overline{\mathrm{OPD}}^{(k)}_{\mathrm{SA(LLT)}} - \overline{\mathrm{OPD}}^{(l)}_{\mathrm{SA(LLT)}}\right]^2 \right\rangle \tag{A4}$$

$$= \left[C_{\overline{\mathrm{OPD}}_{\mathrm{SA(LLT)}}}\right]_{kk} + \left[C_{\overline{\mathrm{OPD}}_{\mathrm{SA(LLT)}}}\right]_{ll} - 2\left[C_{\overline{\mathrm{OPD}}_{\mathrm{SA(LLT)}}}\right]_{kl}, \tag{A5}$$

where the covariance matrix elements are given by

$$\left[C_{\overline{\mathrm{OPD}}_{\mathrm{SA(LLT)}}}\right]_{kl} = -\frac{1}{2}\left[P_{\mathrm{SA(LLT)}} D_{\mathrm{OPD}_{\mathrm{SA(LLT)}}} P^{\mathrm{T}}_{\mathrm{SA(LLT)}}\right]_{kl}, \tag{A6}$$

and $D_{\mathrm{OPD}_{\mathrm{SA(LLT)}}}$ denotes the Kolmogorov shift-invariant OPD structure function matrix, whose elements are equal to

$$\left[D_{\mathrm{OPD}_{\mathrm{SA(LLT)}}}\right]_{kl} = \left\langle \left[\mathrm{OPD}^{(k)}_{\mathrm{SA(LLT)}} - \mathrm{OPD}^{(l)}_{\mathrm{SA(LLT)}}\right]^2 \right\rangle \tag{A7}$$

$$= 6.88\left(\frac{\|\vec{x}^{(k)} - \vec{x}^{(l)}\|}{r_0(\lambda_0)}\right)^{5/3}\left(\frac{\lambda_0}{2\pi}\right)^2. \tag{A8}$$

The 2D correlation integral defining the short-exposure OTFs given in Eq. (7) is then computed for all spatial shifts $(\lambda u_x, \lambda u_y)$ from Eq. (A4).

The authors thank the Purple Crow Lidar team from the University of Western Ontaria, Canada, for making their sodium layer measurements available to us. The authors also thank Glen Herriot and Jean-Pierre Véran from the Herzberg Institute of Astronomy, Canada, for fruitful discussions. The authors acknowledge the support of the TMT partner institutions including the Association of Canadian Universities for Research in Astronomy (ACURA), the Association of Universities for Research in Astronomy (AURA), the California Institute of Technology, and the University of California. This work was also supported by the Canada Foundation for Innovation, the Gordon and Betty Moore Foundation, the National Optical Astronomy Observatory, which is operated by AURA under cooperative agreement with the National Science Foundation, the Ontario Ministry of Research and Innovation, and the National Research Council of Canada.

References and Notes

1. B. L. Ellerbroek, M. Britton, R. Dekany, D. Gavel, G. Herriot, B. Macintosh, and J. Stoesz, "Adaptive Optics for the Thirty Meter Telescope," in *Astronomical Adaptive Optics Systems and Applications II*, R. K. Tyson and M. Lloyd-Hart, eds., Proc. SPIE **5903,** 20–31 (2005).
2. P. S. Argall, R. J. Sica, O. Vassiliev, and M. M. Mwangi, "Lidar measurements taken with a large-aperture liquid mirror: sodium resonance-fluorescence system," Appl. Opt. **39,** 2393–2399 (2000).
3. C. d'Orgeville, F. Rigaut, and B. L. Ellerbroek, "LGS AO photon return simulations and laser requirements for the Gemini LGS AO program," Gemini Observatory preprint #55, available online at www.gemini.edu/documentation/webdocs/preprints/gpre55.pdf.
4. B. L. Ellerbroek and G. M. Cochran, "Wave optics propagation code for multiconjugate adaptive optics," in *Adaptive Optics Systems and Technology II*, R. K. Tyson, D. Donaccini, and M. C. Roggemann, eds., Proc. SPIE **4494,** 104–120 (2002).
5. B. L. Ellerbroek, "Wavefront reconstruction algorithms and simulation results for multiconjugate adaptive optics on giant telescopes," in *Second Backaskog Workshop on Extremely Large Telescopes*, A. L. Ardeberg and T. Andersen, eds., Proc. SPIE **5382,** 478–489 (2004).
6. G. A. Tyler and D. L. Fried, "Image-position error associated with a quadrant detector," J. Opt. Soc. Am. **72,** 804–808 (1982).
7. L. Gilles, "Closed-loop stability and performance analysis of least-squares and minimum-variance control algorithms for multiconjugate adaptive optics," Appl. Opt. **44,** 993–1002 (2005).
8. J. W. Beletic, "Follow the yellow-orange rabbit: a CCD optimized for wavefront sensing a pulsed sodium laser guide star," in *Optical and Infrared Detectors for Astronomy*, J. D. Garnett and J. W. Beletic, eds., Proc. SPIE **5499,** 302–309 (2004).